

## Article

# Assessing Fatigue Life Cycles of Material X10CrMoVNb9-1 through a Combination of Experimental and Finite Element Analysis

Mohammad Ridzwan Bin Abd Rahim <sup>1,2,\*</sup>, Siegfried Schmauder <sup>1</sup>, Yupiter H. P. Manurung <sup>3</sup>, Peter Binkele <sup>1</sup>, Ján Dusza <sup>4</sup>, Tamás Csanádi <sup>4,5</sup>, Meor Iqram Meor Ahmad <sup>6</sup>, Muhd Faiz Mat <sup>3</sup> and Kiarash Jamali Dogahe <sup>1,7</sup>

- <sup>1</sup> Institute for Material Testing, Materials Science and Strength of Materials (IMWF), University of Stuttgart, 70569 Stuttgart, Germany; siegfried.schmauder@imwf.uni-stuttgart.de (S.S.); peter.binkele@imwf.uni-stuttgart.de (P.B.); kiarash.dogahe@imwf.uni-stuttgart.de (K.J.D.)
  - <sup>2</sup> Department of Occupational Safety and Health (DOSHS) Sarawak, Kuching 93100, Malaysia
  - <sup>3</sup> Smart Manufacturing Research Institute (SMRI) and School of Mechanical Engineering, Universiti Teknologi MARA (UiTM), Shah Alam 40450, Malaysia; yupiter.manurung@uitm.edu.my (Y.H.P.M.); muhdfaizmat@uitm.edu.my (M.F.M.)
  - <sup>4</sup> Institute of Materials Research of SAS, Watsonova 47, 040 01 Košice, Slovakia; jdsusza@saske.sk (J.D.); tcsanadi@saske.sk (T.C.)
  - <sup>5</sup> Donát Bánki Faculty of Mechanical and Safety Engineering, Óbuda University, Népszínház utca 8, 1081 Budapest, Hungary
  - <sup>6</sup> Department of Mechanical and Manufacturing Engineering, Faculty of Engineering and Built Environment, Universiti Kebangsaan Malaysia (UKM), Bandar Baru Bangi 43600, Malaysia; meoriqram@ukm.edu.my
  - <sup>7</sup> Graduate School of Advanced Manufacturing Engineering (GSaME), University of Stuttgart, Nobelstraße 12, 70569 Stuttgart, Germany
- \* Correspondence: ridzwan.rahim@imwf.uni-stuttgart.de



**Citation:** Rahim, M.R.B.A.; Schmauder, S.; Manurung, Y.H.P.; Binkele, P.; Dusza, J.; Csanádi, T.; Ahmad, M.I.M.; Mat, M.F.; Dogahe, K.J. Assessing Fatigue Life Cycles of Material X10CrMoVNb9-1 through a Combination of Experimental and Finite Element Analysis. *Metals* **2023**, *13*, 1947. <https://doi.org/10.3390/met13121947>

Academic Editor: Koji Takahashi

Received: 9 October 2023

Revised: 16 November 2023

Accepted: 24 November 2023

Published: 28 November 2023



**Copyright:** © 2023 by the authors. Licensee MDPI, Basel, Switzerland. This article is an open access article distributed under the terms and conditions of the Creative Commons Attribution (CC BY) license (<https://creativecommons.org/licenses/by/4.0/>).

**Abstract:** This paper uses a two-scale material modeling approach to investigate fatigue crack initiation and propagation of the material X10CrMoVNb9-1 (P91) under cyclic loading at room temperature. The Voronoi tessellation method was implemented to generate an artificial microstructure model at the microstructure level, and then, the finite element (FE) method was applied to identify different stress distributions. The stress distributions for multiple artificial microstructures was analyzed by using the physically based Tanaka–Mura model to estimate the number of cycles for crack initiation. Considering the prediction of macro-scale and long-term crack formation, the Paris law was utilized in this research. Experimental work on fatigue life with this material was performed, and good agreement was found with the results obtained in FE modeling. The number of cycles for fatigue crack propagation attains up to a maximum of 40% of the final fatigue lifetime with a typical value of 15% in many cases. This physically based two-scale technique significantly advances fatigue research, particularly in power plants, and paves the way for rapid and low-cost virtual material analysis and fatigue resistance analysis in the context of environmental fatigue applications.

**Keywords:** X10CrMoVNb9-1 (P91); two-scale material modeling (TSMM); Tanaka–Mura model (TMM); Paris law; fatigue life cycles

## 1. Introduction

Power plants have been generating massive quantities of electricity and refining raw materials into final products. The typical life span of a power plant is 402,960 h [1,2]. Low cycle fatigue stresses are imposed on machinery that operates at high temperatures and with some vibration due to its surroundings. Increasing a power plant's operating temperature within the allowed range is a principal means of improving energy efficiency, but it requires remarkable structural integrity [3]. Monitoring structural integrity and detecting local failures are critical for ensuring that respective components remain fit for

service. Understanding a material's fatigue life under cyclic load is essential because structures can collapse under fatigue loading at loads lower than the material's yield stress.

Numerous researchers [4,5] have examined the X10CrMoVNb9-1 P91 steel's high-temperature crack development characteristics under constant load. Saad et al. investigated P91 materials to develop a constitutive viscoplasticity model capable of reproducing the mechanical behavior of power plant materials under thermomechanical fatigue conditions [6]. They discovered that viscoplasticity might be employed in predicting P91 steel behavior at temperatures ranging from 400 °C to 600 °C. Jinbiao et al. investigated the prediction of high-temperature fatigue crack onset in P91 steels [7]. They observed that high-angle grain boundaries were reinforced by 74% when they compared the fine-grain heat-affected zone alongside the coarse-grain heat-affected zone.

The accumulation of damage under cyclic loading is the key issue of fatigue, making it a nuanced phenomenon [8]. The fatigue life of engineering constructions is an intricate process with different phases. To simplify this procedure, engineering structure design often considers three superordinate phases: fracture initiation, fatigue crack propagation, and unstable crack growth. These phases are frequently evaluated separately. Figure 1 shows a graphic representation of the stage of the fatigue life cycle. Zhan investigated the fatigue behavior of TC4-TC11 titanium alloys through laser-melting deposition [9], while Huang et al. adopted a damage mechanics approach to examine the effects of overload on notched specimen fatigue, combining residual stress and plastic damage [10].

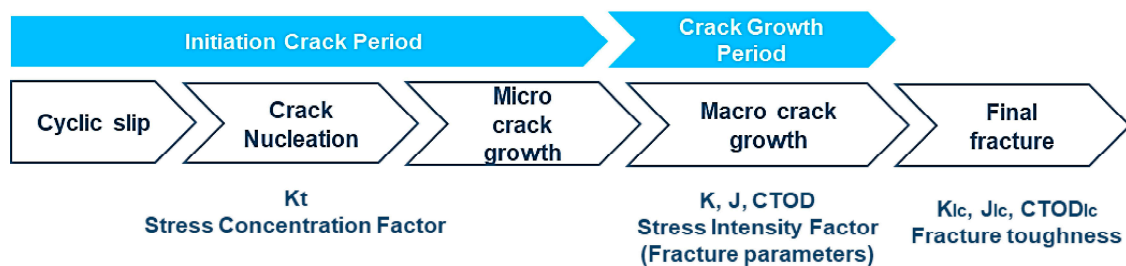


Figure 1. Life cycles of fatigue.

Several researchers [2,11–13] have employed the Tanaka–Mura model (TMM) as a modeling tool to determine the initiation of cracks. The concept was first presented by A. Brückner-Foit and X. Huang [14], who developed a computer model for the evolution of fracture due to fatigue in martensitic steels (F82H) using an updated version of the TMM. Brückner-Foit's research focuses more on quantifying cycles than does Kramberger et al.'s [13] investigation into the segmental crack nucleation process. Mlikota and Schmauder et al. [15] used the improved TMM to establish multiscale modeling and simulation of the metal fatigue method. The researchers estimated the number of cycles needed for the ultimate fracture using a dual-scale and a multiscale framework to assess crack initiation and propagation. They successfully evaluated the simulation of crack initiation with experiments on various steel varieties, including AISI 1141, high-strength steel S960, and martensitic steel.

Santus et al. investigated the development of small metal cracks [16]. They discovered that crack development has three stages. The first stage is the microstructurally short crack (MSC) stage, which raises questions about the applicability of continuum mechanics when the crack dimension is equivalent to or less than the grain size. The second stage is the physically short crack (PSC) stage, in which the crack barely grows due to reduced closure and other influences. The final stage is the long crack (LC) stage, in which the crack continues to develop following the Paris law until it ultimately fractures.

Following Tanaka and Mura's argument [17,18], a dislocation model that incorporates a double pile-up positioned on a single slip band effectively captures the inception phase of the crack. The interaction between forward and reverse loading results in fatigue, and over time, materials exhibit flaws, such as dislocations. As the cycles increase, new crystals

show evidence of slip bands, and the existing bands widen, with some eventually evolving into short cracks. The slip band or slip lines initially appear in a few well-aligned crystals (grains) within the substructure as narrow and sharp lines. In most metals, the slip systems are numerous, and the active ones are oriented close to the planes with the maximum shear stress. When a force is applied in only one direction (uniaxial loading), the crack planes will always be angled at an estimated  $45^\circ$ .

The Paris law frequently illustrates the propagation of long cracks (as shown in Equation (1)). It develops a relationship with the stress intensity factor (SIF)  $K$ , which occurs at the crack's tip during the steady crack growth duration and the fatigue crack growth rate, which is also known as FCGR or  $da/dN$  [19,20].

$$da/dN = C(\Delta K)^m \quad (1)$$

The constants obtained via experimentation are  $C$  and  $m$ . The equation formally describes an experiment on the formation of fatigue cracks. An essential detail to recognize is that physical laws guide the development of fatigue cracks. The relationship between the crack growth rate ( $da/dN$ ) and the stress intensity factor range ( $\Delta K$ ) curve is where the Paris law is applied, as shown in Figure 2. The mechanism that causes the fracture to propagate is pushed by the crack driving force. This specific force is related to the value of the critical SIF  $\Delta K_{Ic}$ .

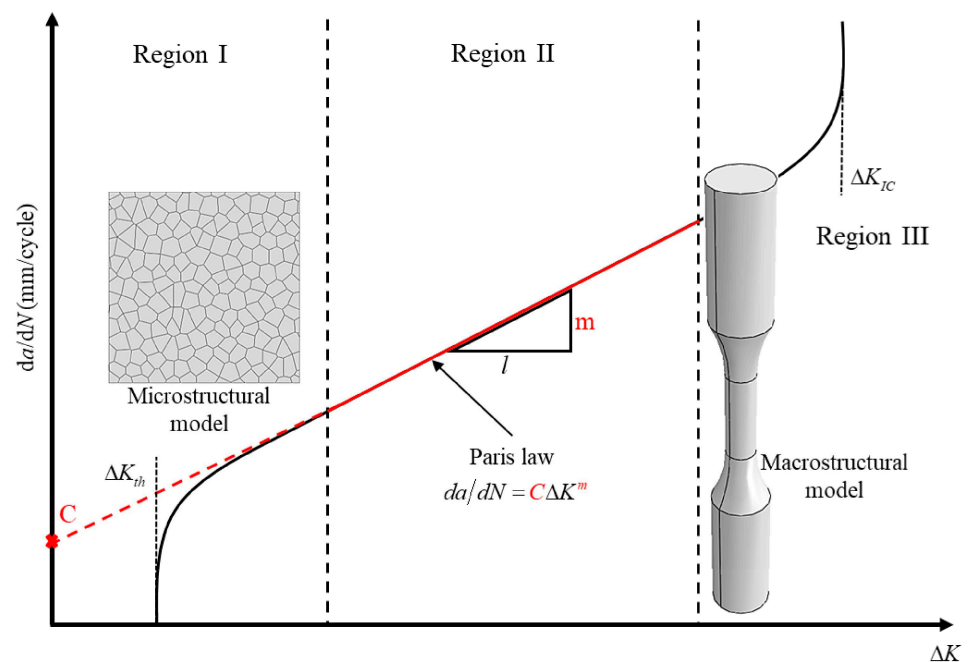


**Figure 2.**  $da/dN$  vs.  $\Delta K$  plot describing the three regions and influencing factors associated with crack growth rate.

In the microstructural study field, few investigations focus explicitly on the material X10CrMoVNb9-1 (P91) that analyze the initiation of short cracks in fatigue. The integration of the Voronoi tessellation (VT) technique with the TMM at the microstructure level, particularly for the P91 material, provides a novel approach to understanding the material's fatigue behavior, particularly regarding crack initiation and propagation in elastic–plastic modeling [7]. The steps of crack initiation and propagation are different, which is why the entire fatigue lifetime needs to be understood and the evaluation of the crack initiation and growing processes needs to be compared through experiments. The physical TMM [11] determines how many cycles a single grain needs to start to microcrack. This analytical model is evaluated numerically and is based on the physical principles of dislocation movement. Three artificial microstructure models were created for this investigation using

the VT technique at room temperature. Simulation findings will be reviewed and discussed for conclusions and recommendations.

## 2. Methodology

### 2.1. P91 Material

The P91 material is a corrosion-resistant steel, whose principal alloying components are approximately 0.1% carbon, 9.0% chromium, and 1.0% molybdenum. This structure includes micro-alloying components such as vanadium and niobium in addition to manganese and silicon. These substances produce MX thermally resistant carbides and carbonitride, particularly V (C,N) and Nb (C,N). At high temperatures, the high strength results from the interaction between these precipitates and dislocations in the matrix. P91 is typically utilized in its hardened state. M23C6 carbides stabilize the structure by locating themselves within grains and sub-grains [21–23]. The high chromium concentration of P91 is partly responsible for its excellent oxidation resistance. Through solid solution hardening, manganese and silicon contribute to an increase in mechanical strength. The chemical composition of the specifications and the investigated heat are detailed in Table 1.

**Table 1.** Mechanical characteristics of P91 material at ambient temperature.

Mechanical Properties (Data from Ref. [24])	24 °C
Shear modulus, G (MPa)	78,986
Poisson's ratio, $\nu$	0.38
Young's modulus, E (MPa)	218,000
Yield stress (MPa)	550
Ultimate tensile stress (MPa)	690

Martensitic steel in its 9Cr-1Mo (P91) form is the substance used in this study, according to ASME Section II and the experimental results. Table 1 displays the material's mechanical properties [24], and Table 2 displays its chemical composition [4].

Electron backscatter diffraction (EBSD) (Figure 3b) was performed to observe the crystallographic orientation and shape of the grains of the microstructure of P91. Three representative microstructures were used to obtain better fatigue crack initiation results, as in Figure 3c.

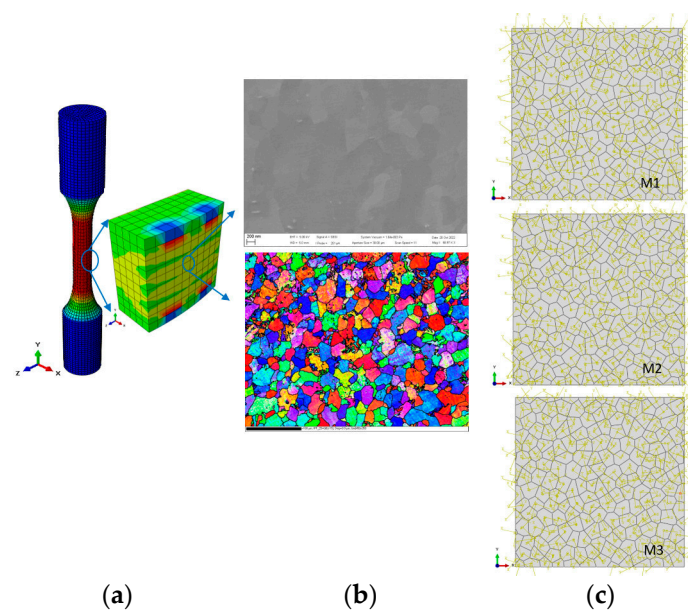


**Figure 3.** Two-scale models illustrating macrostructure as a global model and 3D submodel (a), SEM and EBSD image (b), and three artificial microstructures (submodel) derived from EBSD image (c).

**Table 2.** Chemical composition of P91 steel in wt%.

Chemical Composition in Mass (%) (Data from Ref. [4])													
	C	Si	Mn	P	S	Cr	Mo	Ti	V	Nb	Ni	N	Al
Minimum	0.09	0.26	0.37	0.15	0.0	0.88	0.91	0.01	0.20	0.08	0.08	0.44	0.01

## 2.2. Experimental Procedure

The experimental approach was used to determine the number of fatigue cycles that X10CrMoVNb9-1 can withstand at room temperature. The specimens for the fatigue test were made of P91 steel (yield stress = 550 MPa; tensile strength = 690 MPa; elongation = 46%). Table 2 displays the chemical composition of the material. This steel is frequently used to create different structural components for power plants, such as superheaters and steam pipelines that can operate up to 600 °C. The samples were taken from a tube with a 57.0 mm diameter and 15.6 mm wall thickness.

The fatigue test was performed at ambient temperature and used constant strain and stress amplitudes. An Instron 8502, from INSTRON (Norwood, MA, USA), testing machine with additional parts for low-cycle testing at room temperature was used for these tests, Figure 4. The stress amplitude-controlled testing used four unique total stress amplitude levels, namely, 300, 425, 475, and 558 MPa. The parameters related to every fatigue test are listed in detail in Table 1. The loading frequency was held constant at 0.5 Hz across all experiments. Instantaneous loads were imposed on the specimens, and the consequent fatigue cycles were measured. The loading ratio (R) was set as  $-1$  and the specimen dimensions as in Figure 5.

The procedure follows ASTM E606-04 standards for strain-controlled fatigue testing [25].



**Figure 4.** Specimen during the fatigue test.

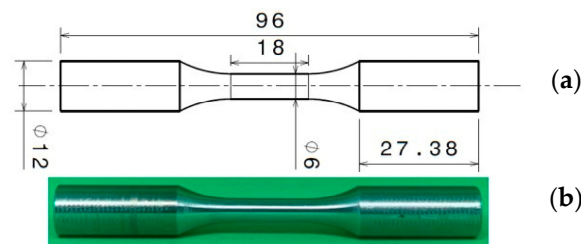


**Figure 5.** (a): Sketch and dimension (unit in millimeters); (b): actual experimental fatigue specimen.

### 2.3. Modeling Fatigue via Elastic–Plastic Analysis

TMM helps to determine how many cycles are needed for cracks to start and grow in individual grains. The crack-initiation stress-number (S-N) of cycles curves estimate how many cycles a crack will last before it breaks. The material being investigated in this study, 9Cr-1Mo (P91), has a body-centered cubic crystal structure [26] and is commonly utilized when high temperatures are involved. The fatigue life curve was derived by assessing the number of cycles required for the initiation of short cracks across varying microstructures. An enhancement over previous studies is the incorporation of plasticity, better aligning the model's characteristics with the real material properties. This adjustment is particularly relevant because it accounts for crack initiation, marking the onset of irreversible material deformation.

The deformation of the elastic–plastic model can be divided into an elastic part and an inelastic (plastic) part. This statement is written as Equation (2):

$$\mathbf{F} = \mathbf{F}^{el} \bullet \mathbf{F}^{pl} \quad (2)$$

where  $\mathbf{F}$  is the total deformation gradient;  $\mathbf{F}^{el}$  is the fully recoverable part of the deformation at the point under consideration ( $[\mathbf{F}^{el}]^{-1}$  is the deformation that would occur if, after the deformation  $\mathbf{F}$ , inelastic responses were somehow prevented, but at the same time, the stress at the point was reduced to zero);  $\mathbf{F}^{pl}$  is defined by  $\mathbf{F}^{pl} = [\mathbf{F}^{el}]^{-1} \bullet \mathbf{F}$  [27]. We consider the slip mechanisms in the microscale as a constitutive model for crystal plasticity. Consequently, the critical resolved shear stress (CRSS) is incorporated into the TMM equation.

### 2.4. Fatigue Crack Initiation Model

In 1981, Tanaka and Mura developed a dislocation model [18,19] that included a dual pile-up formation on a single slip plane to explain how cracks nucleate. The number of fatigue crack initiations needs to be determined before calculating the total number of cycles for fracture due to fatigue. Crack nucleation inside a single grain can be predicted using the TMM, as indicated in Equation (3):

$$N_g = \frac{8GW_c}{\pi(1-v)d(\Delta\bar{\tau} - 2CRSS)^2} \quad (3)$$

where  $N_g$  is the number of cycles for fatigue crack initiation,  $G$  is the shear modulus,  $W_c$  is the specific fracture energy per unit area,  $v$  is the Poisson's ratio,  $d$  is the length of the slip band,  $\Delta\bar{\tau}$  is the average shear stress range on the slip band, and CRSS stands for critical resolved shear stress, which is the critical value of shear stress in the glide direction, whereby the dislocation movement can occur. Grain boundary dislocation pile-up is prevented if the resolved shear stress is smaller than the CRSS.

### 2.5. Fatigue Crack Propagation

The growth rate of prolonged fatigue cracks (stated as  $da/dN$ ) at particular stress conditions for a wide range of technical alloys is generally defined by the Paris law [28], which is a widely recognized theory based on linear elastic fracture mechanics (LEFM):

$$\frac{da}{dN} = C(\Delta K)^m \tag{4}$$

where  $da/dN$  is the crack growth rate,  $\Delta K = K_{\max} - K_{\min}$  is the SIF range at the crack tip during stable crack growth, and C and m are (the Paris) constants of the material that can be inferred via fitting to experimental data or computed mathematically, respectively [29].

Figure 11 shows how the  $a - N$  curve can be utilized to determine the number of cycles needed for an LC to propagate,  $N_{prop}$ , spanning from the point at which crack initiation is complete,  $a_0$ , to the eventual failure point and  $a_f$  of a specimen or component. This curve can be obtained by integrating a power-law equation, such as [30]:

$$N(a) = \frac{1}{C} \int_{a_0}^{a_f} \frac{da}{(\Delta K)^m} \tag{5}$$

In terms of the final failure, the  $a - N$  curve and fracture toughness,  $\Delta K$ , have an impact such that  $N_{prop} = f(Na, K_{Ic})$ . The Paris law and its amendments [31] should be noted as the sole set of criteria that can be used to determine the durability of structural components with early cracks.

A numerically based S-N (Wöhler) curve can be created by integrating the results from the TMM and the Paris law (Equations (1) and (3)), and it can be used to predict when the final failure can be expected to happen for various loading levels.

### 2.6. Physical Model

A physical model represents a real model of an object or system. It is designed to represent, simulate, or predict the behavior of the actual object or system in the real world. This model is applied when conducting experiments or gathering data would be impractical, costly, or impossible. Numerical simulations of crack initiation were carried out using ABAQUS [32], which included a plug-in for the TMM and VT, to specifically address micro-crack nucleation. The ABAQUS scripting interface is used by the Python code that invokes the graphical user interface [33]. The execution, in this case, consists of two parts: Python programming, which manages and directs the simulation procedure, and ABAQUS, which handles tasks such as pre-processing, solving the actual finite element (FE) problems, and post-processing (Figure 6).

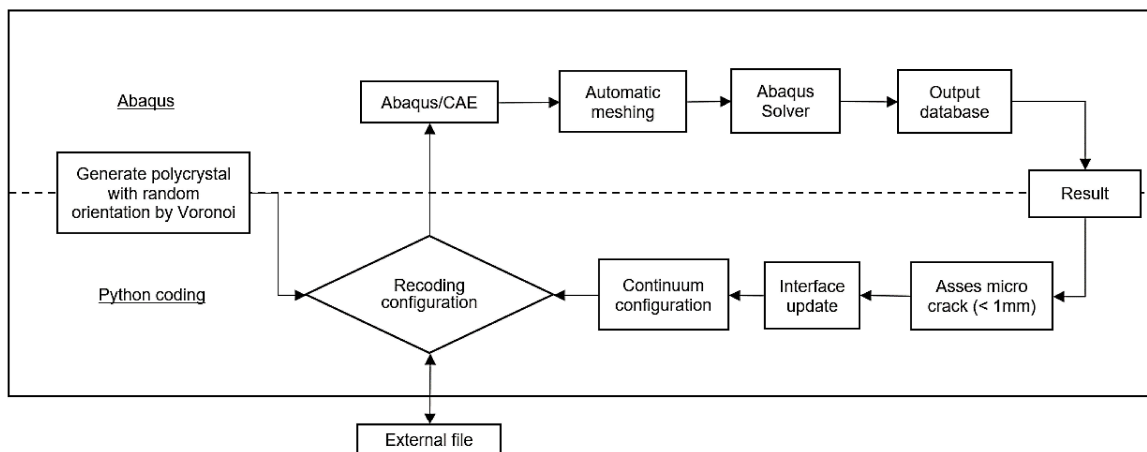


Figure 6. Algorithm for evaluating the number of initiation cycles during the crack initiation phase.

Figure 6 depicts the algorithm for evaluating fatigue crack initiation. The initial stage involves the development of a polycrystalline microstructure. This process requires four main parameters in VT, namely, seeds, perturbation, grain size, and boundary. Seeds are starting points for the initiation of grain structure, perturbation is a slight displacement to these seeds to ensure randomness and mimic natural microstructure variations, grain size is the average size of the grains, and grain boundaries refer to the outline of the simulated microstructure and the interface between grains. The micro-model is derived based on VT to simulate the assembly of polycrystalline grains. Each grain's displacement field in the micro-model, which collectively represents an infinite variety of orientations, is used to calculate the characteristics of the boundary interface. An auxiliary file is created with microcrack geometry, slip band, and slide segment properties for every grain. This model serves as the ground zero for the next phase of the crack initiation process.

The model is meshed using the Mesh module in ABAQUS, and the solver provides a database of displacements, strains, and stresses as outputs. The next microcrack in the micro-model can be predicted using a custom-developed routine (Python algorithm) using the shear stress magnitude on each segment. Grain boundaries—representing the grains within the microstructure—are said to have failed if a microcrack forms on an already present slip plane segment.

On the basis of the TMM in Equation (3), the average shear stress on a slip plane,  $\Delta\bar{\tau}$ , must exceed twice the CRSS ( $\Delta\bar{\tau} - 2CRSS$ ) value. This will ensure the activation of the necessary slip systems to identify the most vulnerable segments. The equation's denominator ( $\Delta\bar{\tau} - 2CRSS$ ) provides an indirect justification for this condition. The TMM predicts a slip plane segment fracture that satisfies the criterion and requires the fewest cycles for nucleation. After a new crack that starts at a particular place is added, the microstructural model is remeshed, and the evaluation under further cyclic loading is repeated until no more segments can be cracked.

The microscale model shown in Figure 3c is used to analyze the initiation of fatigue cracks [13]. This model shows that microcrack nucleation models can reliably forecast the beginnings of fatigue cracks. The VT technique creates an extensive microstructure before this model can be used. On the basis of the experimentally acquired EBSD image in Figure 3b, the microstructure of the submodels (M1, M2, and M3) was produced randomly, with an average grain size of 20  $\mu\text{m}$ . X. Yang et al. [34] and Li et al. [35] similarly found 20  $\mu\text{m}$  grain sizes for 9Cr-1Mo at different temperatures.

Representative volume elements (RVEs), which are produced using the VT approach, are a key component of the simulation model. A random orientation is assigned to each cell in the Voronoi structure. Each cell represents a prior martensite grain, which cause the random angles of the cells; thus, the crystal structure orientations in the plane are defined [13]. The Voronoi method correctly represents the average grain size of a material's microstructure. The micro-models of this work typically comprise 104,501 distinct elements and an average of 199 grains. The 3D shell models possess a non-zero thickness and differ from their 2D equivalents in containing non-constant through-thickness stresses. This 3D shell submodel represents a layer of grains in the XY plane with a thickness equal to the average grain size (20  $\mu\text{m}$ ) (Figure 3c).

### 2.7. Evaluation of Short Crack Initiation Wöhler (S-N) Curve Utilizing Numerical Methods

The microstructural model estimates brief fatigue crack nucleation and propagation. Generating the micro-model for fatigue initiation analysis is crucial. This model is carefully placed at the area of maximal stress concentration where crack initiation is expected. In this work, 0.3 mm  $\times$  0.3 mm micro-models with an average grain size that mimics the initiation process were chosen. This scale was selected to balance computational feasibility with the model size that accurately represents physical crack initiation processes. These dimensions were enough to view the crack nucleation. Figure 3c shows the carefully designed artificial microstructure model based on the EBSD image. This scientific approach

gives a granular view of material fatigue behavior, improving our understanding of crack initiation before propagation.

Although the micro-model is generated in 2D in Figure 3c, implementing the M3D4R elements makes the model a three-dimensional deformable shell mesh. This model uses membrane components and simplified integration techniques to reduce computational complexity. One common use of these elements is to model thin stiffening components within a continuum. These components usually act as reinforcing layers in various materials and structure systems.

The micro-models employed in this study exhibit orthotropic elastic–plasticity material properties, which allow an enriched understanding of material behavior, conforming to the requirements in Table 1. The incorporation of plastic properties within the microstructure model marks an enhancement over previous research [2]. This condition represents that the microstructure has direction-dependent properties toward the elastic region and undergoes plastic deformation. Equations (6) and (7) are used to obtain the elastic constants for cubic symmetry, which are then applied to the micro-models and are shown in Table 3. Notably,  $C_{44}$ , as expressed in Equation (8), corresponds to the material’s shear modulus. The CRSS and the crack initiation energy ( $W_c$ ) are the two material parameters included in the TMM, which was used in this study. According to earlier research [35], the  $W_c$  value can be derived from the  $J$ - $R$  curve as derived from experiments or from calculations of a CT specimen. The CRSS, set at 134.5 MPa for this study, was determined by experimental data, the specifics of which will be covered in a subsequent paper.

**Table 3.** Elastic constants for cubic crystal structures applied in the micro-model to characterize the material behavior.

Elastic Properties	Equation of Elastic Constant for Cubic Crystal	Value of Elastic Constant at 24 °C, MPa
$C_{11} = C_{22} = C_{33}$	$C_{11} = \frac{E(1-\nu)}{(1-\nu-2\nu^2)}$ (6)	408,092
$C_{12} = C_{13} = C_{23}$	$C_{12} = \frac{E\nu}{(1-\nu-2\nu^2)}$ (7)	250,121
$C_{44} = C_{55} = C_{66}$	$C_{44} = G = \frac{E\nu}{2(1+\nu)}$ (8)	78,986

### 2.8. Geometry of the Macro-Models

Developing a thorough macro-scale model known as the global model for the specimen is required to create a numerical representation for analyzing crack propagation. This model has two purposes: first, to convey the stress amplitude and as a boundary condition to the microstructure model, and second, to aid in the precise computation of the SIF for crack propagation analysis. The critical SIF would be achieved by adjusting the seam crack length  $a$  on the model using the extended FE method (XFEM).

As demonstrated in Figure 7, the model utilized in this investigation is axisymmetric. Axisymmetric modeling is a type of FE analysis that can be performed within Abaqus under the presumption that the model’s geometry, material properties, and loading conditions are all symmetric about some central axis. This method is also called 2.5D and makes computing much more efficient by letting a rotational symmetric three-dimensional object be shown and studied as a cross-section in two dimensions. A study on mesh convergence guided the determination of mesh density.

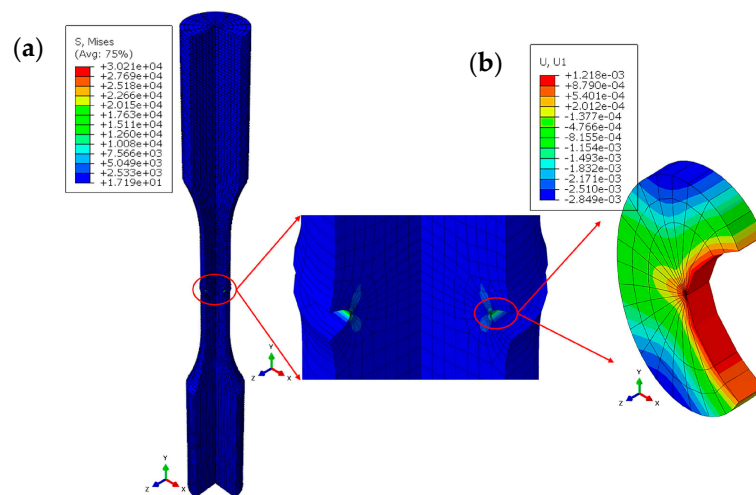


**Figure 7.** The 3D FE model, incorporating symmetrical boundary conditions, utilized to compute the SIF,  $K$  for varying crack lengths: (a) in unit MPa and (b) in unit mm.

### 3. Result and Discussion

On the basis of the EBSD image in Figure 3b, three separate micro-models mirroring a particular microstructure were chosen for the numerical investigation of fatigue crack initiation lifetime. These models were subjected to seven stress amplitudes at room temperature: 300, 350, 400, 425, 475, 524, and 558 MPa. Figure 4 depicts the experimental results obtained by the School of Mechanical Engineering at UiTM Shah Alam, Malaysia, serving as a premise for comparison with the simulated outcomes. The fatigue test with stress amplitudes of 350, 400, and 524 MPa was not conducted experimentally due to the limitation of specimens and to observe the pattern of the number of cycles from TMM. The grains subjected to the maximum stress levels, typically the weakest grains expected to initiate the first MSCs, were identified by using an Abaqus plug-in enhanced with the TMM. Figure 9b shows the microcrack model in which the shear stresses change between grains and within each grain due to the orientation of each grain and the load applied. The TMM Equation (3) indicates that this result means the first microcrack starts along the grain slip line with the shortest expected lifetime.

The average shear stress range ( $\Delta\bar{\tau}$ ) on the slip line, obtained from the FE analysis, is a crucial input in this equation. The local stress field changes once the crack is initiated, making it less tight. The number of cycles required to initiate a new crack is subsequently recalculated for each grain and slip line in the microstructure. Similar to the case where the microstructure is unaffected, the subsequent MSC that needs the fewest cycles to start is found. Then, a crack appears in the RVE. The model was improved to support the sequential nucleation of cracks at the segmental level, which aligns with the improvement described in [12]. In each simulation step, only one slip line segment of a specific grain develops a crack. If a segment from one grain breaks in one stage, then a segment from another grain may probably crack in the next step at the same cycle number or at a higher one. For this change, the TMM equation had to be changed by changing the grain-breaking cycles ( $N_g$ ) to segment-breaking cycles ( $N_s$ ) and the slip line length ( $d$ ) with the slip line segment length ( $d_s$ ) [36,37]. The model was remeshed after creating each segmental crack, and the process was then repeated.

For this investigation, each grain slip line was divided into four equal-sized segments. On the basis of the TMM equation, each MSC or segmental crack that forms in the micro-model has its length and number of life cycles. The crack growth rate is calculated by dividing these two output numbers. Figure 8b shows this crack growth rate when plotted against the number of cracked slip line segments. In all the studied cases, the crack growth rate oscillated and went down after a certain number of cycles. Figure 8b, which depicts the 300 MPa stress amplitude instance, shows this different behavior in action. In the example

under discussion, the state of retardation is indicated by the decreasing and flattening trend of the crack growth rate at the end of the crack initiation period. Similar decreasing trends in small crack growth were documented by Newman et al. [38], as seen in Figure 8a at S1. In Figure 8a, the growth of PSC is represented by the dotted lines, which occur to the left of the LC growth curve, indicated by a solid line. The threshold for long crack growth is defined by the SIF range,  $\Delta K_{th}$ . Values of  $\Delta K$  below this threshold indicate regions where no crack growth is observed.

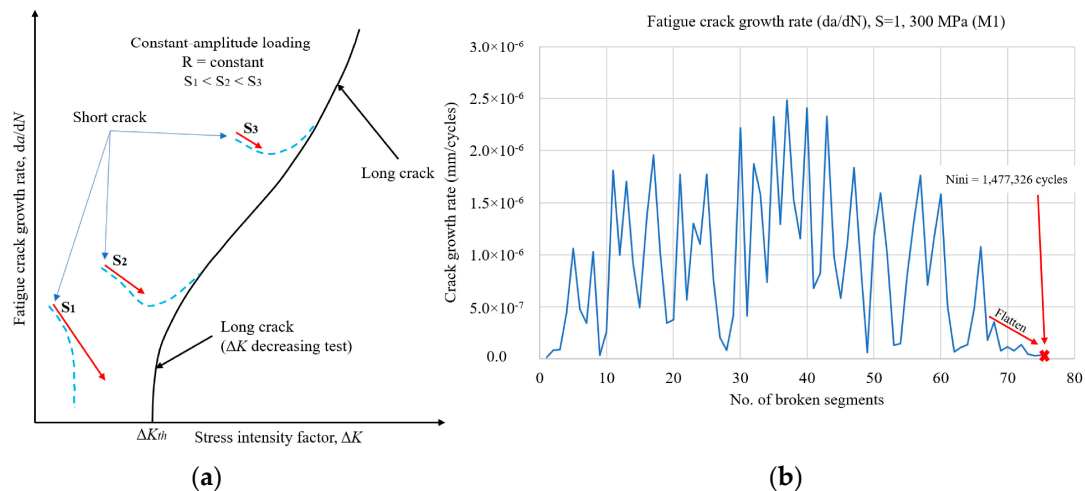


**Figure 8.** (a) Fatigue crack growth for rate for short and long cracks (data from Ref. [38]); (b) fatigue crack growth rate in case of retardation for stress level 300 MPa (M1).

As depicted in Figure 8a, the data points indicate short crack growth declines in the number of cycles and merge with the LC curve at increased loading levels (S2 and S3), as described by Newman et al. [38]. This merging is an indication that the cracks have transitioned from the short crack initiation phase to the LC growth regime. Therefore, the completion of the crack initiation process can be precisely identified at the juncture where the short crack initiation data align with the LC curve, indicating that the behavior of the crack growth has entered the LC propagation stage. The proposed idea is that the crack had changed from the crack initiation stage to the LC growth phase when the crack growth rate reduced noticeably (Figure 9c). As a result, the total number of cycles required for crack initiation could be calculated by adding the cycles required for the nucleation of all segmental cracks until a discernible crack growth rate reduction was noticed. However, at a lower loading point (S1), short cracks may stop growing and not continue propagating to an LC because of the vast number of cycles with shallow  $da/dN$  magnitude. This condition causes the oscillation of the  $da/dN$  to follow the usual downward trend, as shown in Figure 8b. In Figure 8b, the case study conducted at a stress amplitude of 300 MPa demonstrates a flattening trend in the  $da/dN$  graph as it approaches the final data points, indicating crack retardation. The cumulative number of cycles associated with the crack initiation stage in the microstructural model can be determined from the aggregate number of cycles associated with the initiation of each segmental crack. The existence of flattened  $da/dN$  curves demonstrates crack retardation and marks the end of this stage. For the exact situation shown in Figure 8b, 1,477,326 cycles were cumulated. The pattern curve in Figure 8b shows periodic fluctuations in the fatigue crack growth rate, indicating that the crack interacts variably with the material's microstructure. These interactions suggest that different regions of the grains possess a distinct resistance to crack propagation.

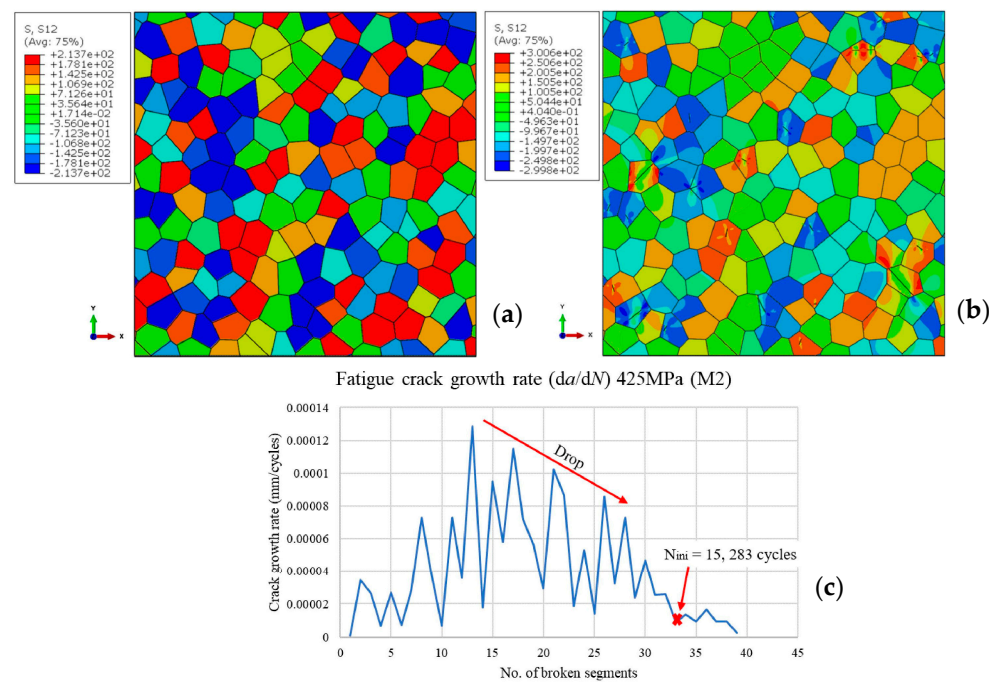


**Figure 9.** (a) Microstructure under a stress of 425 MPa; (b) microstructure depicting scattered crack initiation following 33 iterations; (c) fatigue crack growth rate plotted at 425 MPa stress amplitude.

The micro-model shown in Figure 9b contains a nucleated MSC, in which the shear stress distribution field can also be recognized. The projected number of cycles needed to complete initiation is shown in Figure 9c on the basis of the above conditions. In this specific instance, 15,283 cycles are required for a stress level of 425 MPa at microstructure 2 (M2). Short cracks are defined as those having a depth of less than 1 mm, as stated by Anderson [30]. Most fatigue fractures remain in the short crack phase for the bulk of their lifetime. Thus, learning about the characteristics of these flaws is of great practical importance.

The model illustrates that cracks typically nucleate in a scattered manner according to the damage course, especially in grains with favorable orientations. According to the TMM, crack formation occurs within the grains when the conditions for microcrack nucleation are favorable. Existing crack segments tend to spread along the entire grain, thus causing localized stress relaxation and concentration at their ends. This condition makes it more likely that new cracks will form in the area. The total number of cycles,  $N_{ini}$ , required for the entire crack initiation is equal to the cumulative sum of cycles required for all segmental cracks that form until the observed rate drop, as illustrated in Figure 9c.

As illustrated in Figure 10, a crack initiation Wöhler (S-N) curve has been generated to graphically depict the initiation phase of a fatigue crack under varied stress amplitudes. The curve is a significant improvement over the previous results in [2] due to the addition of plasticity to the global model and the microstructure models.

In the microstructure model, plastic deformation will happen when the material is stressed beyond its elastic limit, leading to crack nucleation. Considering plasticity is essential for understanding and predicting material fatigue under various high, medium, and low loads. The black curve demonstrates the average fatigue crack initiation from three different micro-models with similar grain size predictions for each data point. In the absence of experimental data of the 350, 400, and 524 MPa stress amplitudes, the TMM produced a result that aligned with the overall trend of the Wöhler curve. As seen in Table 4, more than a million cycles at a stress amplitude of 300 MPa occurred during the experiment. The average number of cycles over the three microstructures is 1,479,969, as obtained by the TMM equation, shown in Table 4.

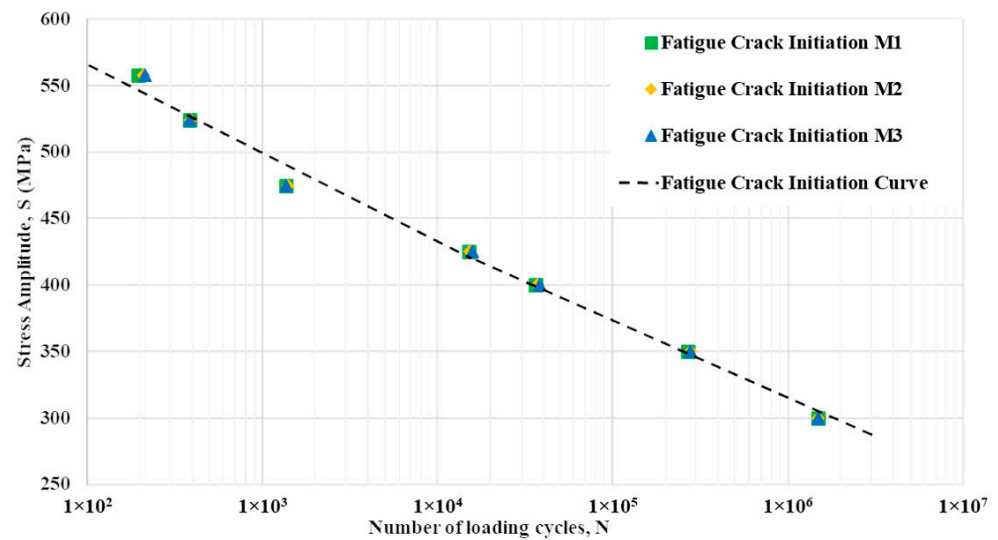


**Figure 10.** Crack initiation Wöhler (S-N) curve for fatigue crack initiation.

**Table 4.** Number of fatigue crack initiation cycles for artificial microstructures and complete fracture from the experimental observation.

Stress Amplitude (MPa)	Number of Cycles for Fatigue Crack Initiation				Number of Cycles for Complete Fracture (Experimental Data at Room Temperature)
	M1	M2	M3	Average	
300	1,477,326	1,479,435	1,480,134	1,479,969	>1 million
350	266,628	277,132	276,872	273,544	Not provided
400	36,223	36,937	38,255	37,138	Not provided
425	15,033	15,283	15,761	15,359	20,944
475	1360	1396	1364	1373	2361
524	394	364	398	385	Not provided
558	194	210	213	206	356

LC propagation was examined using the LFM parameter, the SIF  $K$ . The model presented in Figure 7 calculated this value using the Abaqus-built XFEM. Table 5 contains a part of the  $\Delta K$  values calculated for different crack lengths under a 425 MPa cyclic load. The experimental value of critical SIF  $185.5 \text{ MPa}\sqrt{\text{m}}$  was provided by Materialprüfungsanstalt, Universität Stuttgart [24].

**Table 5.** Critical SIF  $K_{Ic}$  computed for different crack lengths under a 425 MPa stress amplitude.

Crack Length, a (mm)	0.21	0.42	0.44	0.70	0.90	1.19	1.28	1.30	1.301
$K_{Ic}, \text{MPa}\sqrt{\text{m}}$	49.93	74.83	77.07	104.79	127.66	166.06	181.61	184.39	185.84

As shown in Equation (4), incorporating the Paris law approach can estimate the number of cycles required for crack propagation to reach final failure. This procedure is dependent on the  $\Delta K$  values determined in the previous phase. The blue line in Figure 11 is the outcome of this integration for a 425 MPa stress amplitude. In the micromechanical model, the final crack length is determined by summing up the projected lengths of individual crack segments identified in the grains. In order to accurately represent the transition from initiation to the propagation stage, the dimensions of the microstructural model were increased to  $0.5 \text{ mm} \times 0.3 \text{ mm}$ . Based on the micromechanical model's dimensions of  $0.3 \text{ mm} \times 0.3 \text{ mm}$  and the extended microstructure model's dimensions of  $0.5 \text{ mm} \times 0.3 \text{ mm}$ , the initial crack segment length is found to be very similar, namely, 0.21 mm and 0.19 mm, respectively. This accumulation marks the point transition from

micro- to mesomechanical modeling. Within the mesomechanical scale model, the crack length begins at 0.21 mm. Table 5 shows the breakdown of the SIF at different crack lengths.

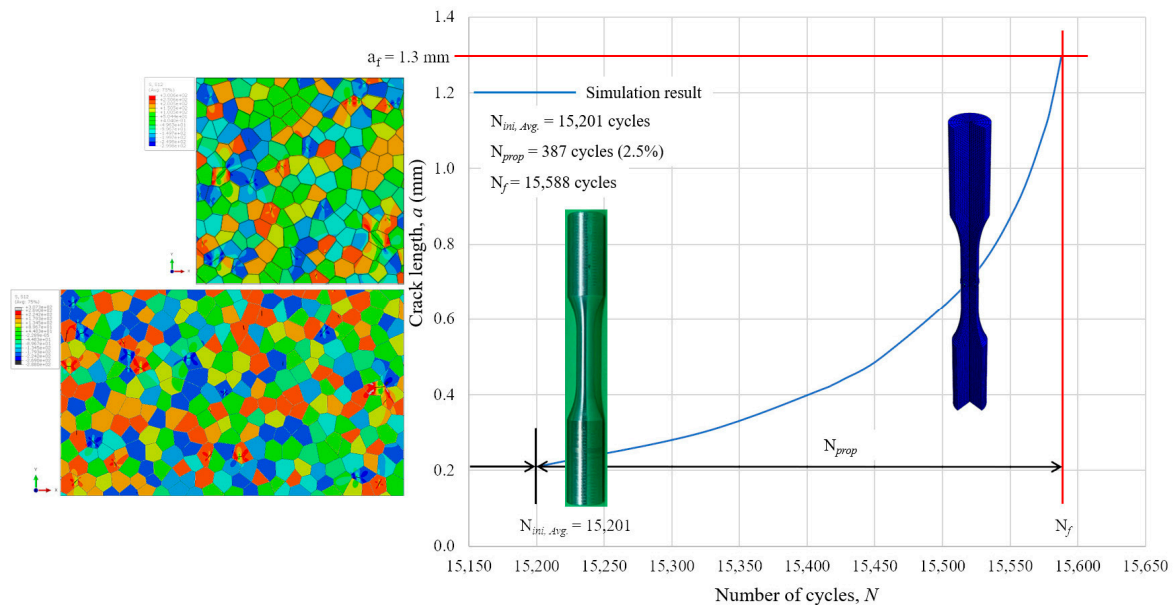


**Figure 11.** Number of cycles of LC growth at 425 MPa.

The critical SIF  $K_{Ic}$  is determined to be  $184.4 \text{ MPa}\sqrt{\text{m}}$  at the crack length of 1.3 mm, which is nearly close to the experimental value mentioned above. The number of cycles it would take for a crack initiation to propagate and cause failure is estimated by using the Paris law. Figure 11 depicts how this was accomplished by drawing a vertical line from the intersection of the  $a - N$  curve (the blue line) and the crack length,  $a_f = 1.3$  mm. The total number of cycles ( $N_f$ ) from both simulations is further explained in Figure 11, including fatigue crack initiation ( $N_{ini, Avg.}$ ) and propagation ( $N_{prop}$ ).

Figure 12 shows an integrated graph exhibiting the stages of fatigue crack initiation (denoted in black curve), fatigue failure curve (depicted in a light blue curve), and the overall number of cycles resulting in fatigue failure as derived from experimental data (represented by red curve). Within statistical tolerances, a difference between 2.5% and 39.0% between the fatigue crack initiation period and propagation phase is acceptable. The apparent difference can be attributed to the stress amplitude applied at the micro and macroscale level; a higher stress amplitude has a pronounced effect on the difference of fatigue crack propagation and fatigue crack initiation. The importance of fatigue crack initiation over fatigue crack propagation in predicting the fatigue life of a material is a crucial finding of this study and has been known for a long time from the literature and for other materials. Short cracks behave very differently from longer cracks during fatigue loading. Another important detail to remember is that the crack initiation phase consumes most of the fatigue life [30]. Additional investigation into the CRSS value is significant to assess its impact on the onset of fatigue crack initiation in the P91 material.

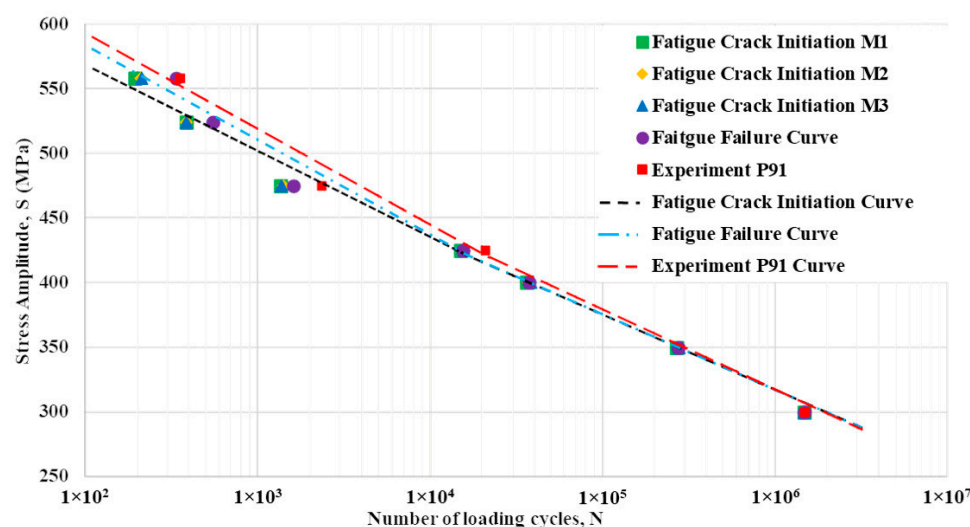


Figure 12. Wöhler curve for fatigue initiation and failure of X10CrMoVNb9-1 (P91).

#### 4. Conclusions

On the basis of the experimental and numerical methods of estimating fatigue life using the TMM and the derivation of the Paris law, predicting fatigue life on the basis of crack initiation and propagation is promising. The following conclusions can be drawn from this work:

- The dimensions of the specimen are in accordance with ASTM E6060-04 standards.
- The local stress field within a component and the material's qualities significantly impact the initiation and development of cracks along slip planes within polycrystalline materials.
- The findings of this study are an improvement over earlier results [2] and have more realistic agreement with the Wöhler curve compared with experimental data in respect to the number of cycles. The enhancement is attributed to incorporating elastic–plastic parameters in the TMM, addressing the previously observed overestimation of cycles for short crack initiation, especially at higher stress levels in the case of neglecting additional continuum plasticity effects in the model.
- This approach offers a way to enhance the durability and dependability of polycrystalline materials in various technical applications and improve the design of their constituent parts.
- The TMM and an artificial microstructure model, in combination with VT, successfully define the fatigue crack initiation location.
- The critical SIF  $K_{Ic}$  can be determined using the 2.5D axisymmetric model. Subsequently, applying the Paris law equation facilitated the calculation of the number of cycles required for fatigue crack propagation. This research emphasizes the crucial roles of the TMM and Paris law in evaluating fatigue life cycles and paves the way for the analyses of fatigue life at elevated temperatures.
- The TMM was applied to artificial microstructure models at high, medium, and low stress levels. Findings show that fatigue crack propagation affects up to 40% of the final lifetime, with a typical effect of around 15% in agreement with standard knowledge also for other materials.

**Author Contributions:** Conceptualization, M.R.B.A.R., S.S. and P.B.; methodology, M.R.B.A.R., S.S., P.B., Y.H.P.M., J.D. and T.C.; software, M.R.B.A.R., S.S. and K.J.D.; validation, M.R.B.A.R., S.S. and Y.H.P.M.; formal analysis, J.D., T.C., M.F.M. and M.I.M.A.; investigation, M.R.B.A.R., S.S., P.B., Y.H.P.M. and T.C.; resources, J.D., T.C. and M.F.M.; data curation, S.S., P.B. and Y.H.P.M.; writing—original draft preparation, M.R.B.A.R.; writing—review and editing, S.S., Y.H.P.M. and M.R.B.A.R.; visualization, M.R.B.A.R. and K.J.D.; supervision, S.S. and Y.H.P.M.; project administration, M.R.B.A.R.; funding acquisition, M.R.B.A.R. All authors have read and agreed to the published version of the manuscript.

**Funding:** This research was funded by the Public Service Department of Malaysia with reference number JPA(I)870614145415. This publication was funded by the German Research Foundation grant, “Open Access Publication Funding/2023-2024/University of Stuttgart” (512689491). Ján Dusza gratefully acknowledge the support of Alexander von Humboldt Foundation.

**Data Availability Statement:** The data presented in this study are available on request from the corresponding author.

**Conflicts of Interest:** The authors declare no conflict of interest.

## References

1. Cui, R.Y.; Hultman, N.; Edwards, M.R.; He, L.; Sen, A.; Surana, K.; McJeon, H.; Iyer, G.; Patel, P.; Yu, S.; et al. Quantifying Operational Lifetimes for Coal Power Plants Under the Paris Goals. *Nat. Commun.* **2019**, *10*, 4759. [[CrossRef](#)] [[PubMed](#)]
2. Rahim, M.R.A.; Schmauder, S.; Manurung, Y.H.P.; Binkele, P.; Ahmad, M.I.M.; Dogahe, K. Cycle Number Estimation Method on Fatigue Crack Initiation using Voronoi Tessellation and the Tanaka Mura Model. *J. Fail. Anal. Prev.* **2023**, *23*, 548–555. [[CrossRef](#)]
3. Abarkan, I.; Khamlichi, A.; Shamass, R. Low Cycle Fatigue Behavior of Circumferentially Notched Specimens Made of Modified 9Cr-1Mo Steel at Elevated Temperature. *Int. Rev. Appl. Sci. Eng.* **2022**, *13*, 54–62. [[CrossRef](#)]
4. Speicher, M.; Klenk, A.; Coleman, K. Creep-Fatigue Interactions in P91 Steel. In Proceedings of the 13th International Conference on Fracture, Beijing, China, 16–21 September 2013.
5. Saxena, A.; Narasimhachary, S. *Creep-Fatigue Crack Growth Testing of P91 Steel: Result of the Round Robin for Assessing ASTM Standard E-2760-10*; EPRI: Palo Alto, CA, USA, 2018; pp. 28–43.
6. Saad, A.A.; Hyde, C.J.; Sun, W.; Hyde, T.H. Thermal-Mechanical Fatigue Simulation of a P91 Steel in a Temperature Range of 400–600 °C. *Mater. High Temp.* **2011**, *28*, 212. [[CrossRef](#)]
7. Zhou, J.; Barrett, R.A.; Leen, S.B. A Physically-Based Method for Predicting High Temperature Fatigue Crack Initiation in P91 Welded Steel. *Int. J. Fatigue* **2021**, *153*, 106480. [[CrossRef](#)]
8. Tahmasbi, K.; Alharthi, F.; Webster, G.; Haghshenas, M. Dynamic Frequency-Dependent Fatigue Damage in Metals: A State-of-the-Art Review. *Forces Mech.* **2023**, *10*, 100167. [[CrossRef](#)]
9. Zhan, Z. Fatigue Life Calculation for TC4-TC11 Titanium Alloy Specimens Fabricated by Laser Melting Deposition. *Theor. Appl. Fract. Mech.* **2018**, *96*, 114–122. [[CrossRef](#)]
10. Huang, J.; Meng, Q.; Zhan, Z.; Hu, W.; Shen, F. Damage Mechanics-Based Approach to Studying Effects of Overload on Fatigue Life of Notched Specimens. *Int. J. Damage Mech.* **2019**, *28*, 538–565. [[CrossRef](#)]
11. Mlikota, M.; Schmauder, S. Multiscale Modelling and Simulation of Metal Fatigue and Its Applications. Ph.D. Thesis, Universität Stuttgart, Stuttgart, Germany, 2020.
12. Jezernik, N.; Kramberger, J.; Lassen, T.; Glodež, S. Numerical Modelling of Fatigue Crack Initiation and Growth of Martensitic Steels. *Fatigue Fract. Eng. Mater. Struct.* **2010**, *33*, 714–723. [[CrossRef](#)]
13. Kramberger, J.; Jezernik, N.; Göncz, P.; Glodež, S. Extension of the Tanaka-Mura Model for Fatigue Crack Initiation in Thermally Cut Martensitic Steels. *Eng. Fract. Mech.* **2010**, *77*, 2040–2050. [[CrossRef](#)]
14. Brückner-Foigt, A.; Huang, X. Numerical Simulation of Micro-crack Initiation of Martensitic Steel under Fatigue Loading. *Int. J. Fatigue* **2006**, *28*, 963–971. [[CrossRef](#)]
15. Mlikota, M.; Schmauder, S.; Božić, Ž. Calculation of the Wöhler (S-N) Curve Using a Two-Scale Model. *Int. J. Fatigue* **2018**, *114*, 289–297. [[CrossRef](#)]
16. Santus, C.; Taylor, D. Physically Short Crack Propagation in Metals During High Cycle Fatigue. *Int. J. Fatigue* **2009**, *31*, 1356–1365. [[CrossRef](#)]
17. Tanaka, K.; Mura, T. A Dislocation Model for Fatigue Crack Initiation. *J. Appl. Mech.* **1981**, *48*, 97–103. [[CrossRef](#)]
18. Tanaka, K.; Mura, T. A Theory of Fatigue Crack Initiation at Inclusions. *Metall. Trans. A* **1982**, *13A*, 117–123. [[CrossRef](#)]
19. Paris, P.C.; Erdogan, F. A Critical Analysis of Crack Propagation Laws. *J. Basic Eng.* **1963**, *84*, 528–533. [[CrossRef](#)]
20. Lesiuk, G.; Smolnicki, M.; Rozumek, D.; Krechkovska, H.; Student, O.; Correia, J.; Mech, R.; Jesus, A.D. Study of the Fatigue Crack Growth in Long-Term Operated Mild Steel under Mixed-Mode (I + II, I + III) Loading Condition. *Materials* **2020**, *13*, 160. [[CrossRef](#)] [[PubMed](#)]
21. Kumar, S.; Varshney, A.; Sangal, S.; Mondal, K. Enhancement of Mechanical Properties of Modified 9Cr-1Mo (P91) Steel Using the Thermomechanical Processing and Smart Heat Treatment Protocol. *Mater. Sci. Eng. A* **2022**, *844*, 143177. [[CrossRef](#)]
22. Sakthivel, T.; Sasikala, G.; Vasudevan, M. Role of Microstructures on Heterogeneous Creep Behaviour Across P91 Steel Weld Joint Assessed by Impression Creep Testing. *Mater. Charact.* **2020**, *159*, 109988. [[CrossRef](#)]
23. Rejeesh, R.; Barik, R.K.; Mitra, R.; Kostryzhev, A.; Das, C.R.; Albert, S.K.; Chakrabarti, D. Effect of B and N Content and Austenitization Temperature on the Tensile and Impact Properties of Modified 9Cr-1Mo Steels. *Metals* **2023**, *13*, 1124. [[CrossRef](#)]
24. Speicher, M. *Versuchsdurchführung in Compliance-technik gemäß MPAS-PA 52220-05; Auftragsabwicklung Bruchmechanikversuch*: Stuttgart, Germany, 2013; p. 1.
25. ASTM Committee E08. *ASTM E606-04: Standard Practice for Strain Controlled Fatigue Testing*; ASTM International: West Conshohocken, PA, USA, 2004; pp. 1–16.

26. Hatakeyama, T.; Sawada, K.; Suzuki, M.; Watanabe, M. Microstructure Development of Modified 9Cr-1Mo Steel During Laser Powder Bed Fusion and Heat Treatment. *Addit. Manuf.* **2023**, *61*, 103350. [CrossRef]
27. 4.2.1 Plasticity Models: General Discussion. Available online: <https://classes.engineering.wustl.edu/2009/spring/mase5513/abaqus/docs/v6.6/books/stm/default.htm?startat=ch04s02ath101.html> (accessed on 26 September 2023).
28. Kujawski, D.; Vasudevan, A.K.; Ricker, R.E.; Sadananda, K. On 50 Years of Fatigue Crack Closure Dispute. *Fatigue Fract. Eng. Mater. Struct.* **2023**, *46*, 2816–2829. [CrossRef]
29. Mlikota, M.; Staib, S.; Schmauder, S.; Božić, Ž. Numerical Determination of Paris Law Constants for Carbon Steel Using a Two-Scale Model. *J. Phys. Conf. Ser.* **2017**, *843*, 012042. [CrossRef]
30. Anderson, T.L. *Fracture Mechanics: Fundamental and Applications, 4th ed*; CRC Press Taylor & Francis Group: Boca Raton, FL, USA, 2017; pp. 473–476.
31. Broek, D. *The Practical Use of Fracture Mechanics*, 3rd ed.; Kluwer Academic Publishers: Dordrecht, The Netherlands, 1997; pp. 123–166.
32. Abaqus 6.13: Theory Guide. Available online: <http://130.149.89.49:2080/v6.13/books/stm/default.htm> (accessed on 26 September 2023).
33. Abaqus Scripting Reference Guide. Available online: <http://130.149.89.49:2080/v6.13/books/ker/default.htm> (accessed on 26 September 2023).
34. Yang, X.; Shi, C.; Cao, H.; Sun, S.; Liu, G. Study on Intelligent Classification of Aging Heat-Resistant Materials. *ACS Omega* **2023**, *8*, 5300–5305. [CrossRef] [PubMed]
35. Li, D.F.; Golden, B.J.; O’Dowd, N.P. Multiscale Modelling of Mechanical Response in a Martensitic Steel: A Micromechanical and Length-Scale-Dependent Framework for Precipitate Hardening. *Acta Mater.* **2014**, *80*, 445–456. [CrossRef]
36. Mlikota, M.; Schmauder, S.; Hummel, M. Modelling of Overload Effects on Fatigue Crack Initiation in Case of Carbon Steel. *Fatigue Fract. Eng. Mater. Struct.* **2017**, *40*, 1182–1190. [CrossRef]
37. Dogahe, K.J.; Guski, V.; Mlikota, M.; Schmauder, S.; Holweger, W.; Spiller, J.J.; Mayer, J.; Schwedt, A.; Görlach, B.; Wranik, J. Simulation of the Fatigue Crack Initiation in SAE 52100 Martensitic Hardened Bearing Steel During Rolling Contact. *Lubricants* **2022**, *10*, 62. [CrossRef]
38. Newman, J.C., Jr.; Phillips, E.P.; Swain, M.H. Fatigue-Life Prediction Methodology Using Small-Crack Theory. *Int. J. Fatigue* **1999**, *21*, 109–119. [CrossRef]

**Disclaimer/Publisher’s Note:** The statements, opinions and data contained in all publications are solely those of the individual author(s) and contributor(s) and not of MDPI and/or the editor(s). MDPI and/or the editor(s) disclaim responsibility for any injury to people or property resulting from any ideas, methods, instructions or products referred to in the content.